



Mind-the-gap part I: Accurately locating warm marine boundary layer clouds and precipitation using spaceborne radars

Katia Lamer^{1*,2**}, Pavlos Kollias^{2,3,4}, Alessandro Battaglia^{5,6} and Simon Preval⁵

¹ City University of New York affiliation

² Brookhaven National Laboratory

³ Stony Brook University

⁴ Cologne University

⁵ University of Leicester, Leicester, UK

⁶ UK National Centre for Earth Observation

* Affiliation when work was conducted

** Current affiliation

Correspondence to: Katia Lamer (klamer@bnl.gov)

1

2 **Abstract**

3

4 Ground-based radar observations show that, in the eastern north Atlantic, 50% of warm marine boundary layer
5 (WMBL) hydrometeors occur below 1.2km and have reflectivities < -17dBZ, thus making their detection from space
6 susceptible to the extent of surface clutter and radar sensitivity.

7

8 Surface clutter limits the CloudSat-Cloud Precipitation Radar (CPR)'s ability to observe true cloud base in ~52% of
9 the cloudy columns it detects and true virga base in ~80%, meaning the CloudSat-CPR often provides an incomplete
10 view of even the clouds it does detect. Using forward-simulations, we determine that a 250-m resolution radar would
11 most accurately capture the boundaries of WMBL clouds and precipitation; That being said, because of sensitivity
12 limitations, such a radar would suffer from cloud cover biases similar to those of the CloudSat-CPR.

13

14 Overpass observations and forward-simulations indicate that the CloudSat-CPR fails to detect 29-41% of the cloudy
15 columns detected by the ground-based sensors. Out of all configurations tested, the 7 dB more sensitive EarthCARE-
16 CPR performs best (only missing 9.0% of cloudy columns) indicating that improving radar sensitivity is more
17 important than shortening surface clutter for observing cloud cover. However, because 50% of WMBL systems are
18 thinner than 400 m, they tend to be artificially stretched by long sensitive radar pulses; hence the EarthCARE-CPR
19 overestimation of cloud top height and hydrometeor fraction.

20

21 Thus, it is recommended that the next generation of space-borne radars targeting WMBL science shall operate
22 interlaced pulse modes including both a highly sensitive long-pulse and a less sensitive but clutter limiting short-pulse
23 mode.



24 **1 Introduction**

25

26 Because of their ubiquitous nature and of the way they interact with solar and longwave radiation, warm marine
27 boundary layer (WMBL) clouds play a crucial role in the global energy budget [Klein and Hartmann, 1993].
28 Unfortunately, numerical models still struggle to properly represent their coverage, vertical distribution, and
29 brightness (e.g., [Nam et al., 2012]). This uncertainty ultimately affects our confidence in future climate projections
30 [Bony et al., 2015; Sherwood et al., 2014]. Climate simulations could be improved from comparisons with additional
31 observations of the macrophysical and microphysical properties of WMBL clouds, as well as from improvements in
32 our understanding of the relationships between low-level clouds and their environment.

33

34 Millimeter-wavelength radar signals, because of their ability to penetrate clouds, have long been used to document
35 the vertical distribution of WMBL clouds (e.g., [Haynes et al., 2011; Sassen and Wang, 2008]) and their internal
36 structure (e.g., [Bretherton et al., 2010; Dong and Mace, 2003; Huang et al., 2012; Lamer et al., 2015]) as well as to
37 identify precipitation (e.g., [Ellis et al., 2009; Leon et al., 2008; Rapp et al., 2013]) and characterize its vertical
38 structure (e.g., [Burleyson et al., 2013; Comstock et al., 2005; Frisch et al., 1995; Kollias et al., 2011]). However, the
39 representativeness of radar observations largely depends on factors such as coverage, radar sensitivity,
40 vertical/horizontal resolution and on the presence of clutter.

41

42 Spaceborne radars are often preferred over ground-based and airborne ones because of their ability to cover vast areas
43 of the globe [Battaglia et al., Submitted]. The first spaceborne Cloud Precipitation Radar (CPR) designed to detail the
44 vertical structure of clouds was launched in 2006 onboard CloudSat [Stephens et al., 2002]. The CloudSat-CPR is still
45 operational; it transmits a 3.3 microsecond pulse with a 1.4 km field of view at the surface and can achieve a sensitivity
46 of -28 dBZ after its measurements are averaged in 0.32-s time intervals and sampled at 0.16-s along its nadir track
47 [Stephens et al., 2002]. However, the CloudSat-CPR's long power pulse also generates a surface clutter echo which
48 tends to partially mask signals from cloud and precipitation forming below circa 1 km [Marchand et al., 2008]. For
49 this reason, the CloudSat-CPR's actual ability to document WMBL clouds and precipitation remains uncertain.

50

51 Comparison of various satellite-based cloud products suggest that globally the CloudSat-CPR can only detects roughly
52 30-50% of all WMBL cloud-containing atmospheric columns [Christensen et al., 2013; Liu et al., 2018; Liu et al.,
53 2016; Rapp et al., 2013]. According to Christensen et al. [2013] most of the CloudSat-CPR cloud cover bias is due to
54 its inability to detect clouds forming entirely within the region occupied by its surface clutter. Rapp et al. [2013]
55 instead attribute this deficiency mainly to the CloudSat-CPR's sensitivity which they believe is insufficient to detect
56 the small droplets composing WMBL clouds like those forming in the southeastern Pacific region. However, in
57 another study, Liu et al. [2018] concluded that the coarse resolution of the CloudSat-CPR has more of an impact on
58 its ability to detect all cloudy columns than surface clutter and limited sensitivity. Such a lack of consensus makes
59 designing more effective radar architectures for future spaceborne missions more complicated. Also, because most
60 existing CloudSat-CPR-performance assessments are based on observations from (visible) sensors that cannot



61 penetrate cloud top, there is little to no information about the CloudSat-CPR's ability to holistically document the
62 vertical structure of those cloudy columns it detects (i.e., provide information from cloud top to cloud base and of
63 virga and rain below cloud).

64

65 It is not uncommon to rely on observations collected by highly sensitive airborne and ground-based millimeter radar
66 observations to assess the performance of coarser less sensitive radars (e.g., [Burns *et al.*, 2016; Lamer and Kollias,
67 2015]). Such observations have allowed Stephens *et al.* [2002] to conclude that, based-on sensitivity alone, the
68 CloudSat-CPR should only be able to detect 70% of marine boundary layer cloud segments. A study considering the
69 impact of the CloudSat-CPR's rather coarse vertical resolution, large horizontal field of view and surface clutter would
70 complement this preliminary work and allow for a more rigorous quantification of its ability to document the vertical
71 distribution of cloud fraction.

72

73 Instrument geometry effects are best accounted for in forward simulators. Using ground-based observations and an
74 instrument forward-simulator Burns *et al.* [2016] determined that the CloudSat-CPR's successor, the EarthCARE-
75 CPR [Illingworth *et al.*, 2015], will only detect 70-80% of marine boundary layer cloud segments; moreover its coarse
76 vertical resolution (500 m, same as the CloudSat-CPR) will introduce significant biases in reported cloud boundaries.
77 These results however likely need be revised since changes have since been made to the design of this joint European
78 Space Agency (ESA) and Japanese Aerospace Exploration Agency (JAXA) spaceborne mission
79 (<https://earth.esa.int/web/guest/missions/esa-future-missions/earthcare>).

80

81 Along those lines, the current study relies on the use of instrument forward simulators and on observations collected
82 by the ground-based Ka-band ARM Zenith radar (KAZR) and the ceilometer operating at the Atmospheric Radiation
83 Measurements (ARM) program Eastern North Atlantic (ENA) facility to document the properties of WMBL clouds
84 and precipitation with the goal of:

85

- 86 ○ quantifying the CloudSat-CPR's ability to estimate their coverage and vertical distribution as well as
87 its accuracy in determining the location of cloud tops and cloud/virga base (Sect. 3.0);
- 88
- 89 ○ identifying which property (thickness, reflectivity, vertical location) of WMBL clouds and
90 precipitation mostly complicate their detection from space (Sect. 4.0);
- 91
- 92 ○ evaluating the performance of alternative radar configurations designed for an optimum
93 characterization of WMBL clouds and precipitation (Sect. 5.0).

94

95 **2 Datasets**

96

97 This study focuses on evaluating how well spaceborne CPR are able to document the properties of warm marine
98 boundary layer (WMBL) clouds. We define WMBL clouds as cloudy columns with the highest cloud top below 5.5



99 km/500 mb and warmer than 0°C. This definition limits our analysis to WMBL regimes not associated with mid- or
100 high- clouds aloft but does not exclude periods where multiple WMBL cloud layers overlap.

101

102 The next sub-sections describe how we extracted cloud and precipitation information from raw CloudSat-CPR – to
103 evaluate the performance of current spaceborne sensors in this regime – (Sect. 2.1), ARM measurements – which act
104 as a benchmark – (Sect. 2.2) and how we forward-simulate alternative spaceborne radar configurations (Sect. 2.3).

105

106 **2.1 CloudSat Spaceborne W-band Radar Observations**

107

108 The CloudSat-CPR has been collecting observations since May 2006; Initially twice a day, but then only once a day
109 (at 15:00 UTC) after it returned to the A-Train in May 2012 following a spacecraft battery failure [Stephens *et al.*,
110 2018]. Periods when CloudSat passed within a 200 km radius of the ARM ENA ground-based facility are used to
111 evaluate the CloudSat-CPR’s ability to characterize WMBL clouds and precipitation (results presented in Sect. 3.0);
112 this happened 117 times since the ground-based site was made permanent at the end of 2015 (daytime only). The
113 GEOPROF granules (algorithm version 4.0) corresponding to these overpasses were identified and extracted for
114 analysis following the method of Protat *et al.* [2009]. Variables taken from this product include Radar_Reflectivity,
115 CPR_Cloud_mask (hydrometeor echo mask), and CPR_Echo_Top (cloud type classification). An example of raw
116 radar reflectivity observations collected by the CloudSat-CPR on February 27, 2016 is given in Fig. 1c.

117

118 The GEOPROF product provides observations sampled every ~240 m in range and ~1.0 km along-track taken from
119 the CloudSat-CPR native 500-m range resolution and ~1.7km along-track by 1.3km across-track field of view
120 [Stephens *et al.*, 2002; Tanelli *et al.*, 2008]. The CloudSat-CPR’s raw radar reflectivity measurements are filtered for
121 clutter and noise using the CPR_Cloud_mask. Progressively more aggressive masks are applied until a compromise
122 is reached between the number of detectable hydrometeors and the amount of remaining noise. Radar reflectivities are
123 first masked for bad and missing echoes (mask value -9; Fig. 1d), then for echoes with significant return power likely
124 affected by - or resulting from- surface clutter (mask value 5; Fig. 1e). Comparison of Fig. 1d and 1e illustrate that a
125 majority of the hydrometeor echoes with significant return power are deemed affected by the surface clutter echo and
126 that following their removal the CloudSat-CPR’s ability to detect clouds and precipitation appears significantly
127 reduced. Since further removing echoes labeled as very weak (mask value 6-20) helps clean up the remaining radar
128 reflectivity time-height image while minimally affecting the number of detected hydrometeor echoes, our evaluation
129 of the CloudSat-CPR’s performance is based only on echoes deemed weak to strong (mask value ≥ 20 ; Fig. 1f).
130 According to estimates by Marchand *et al.* [2008] these echoes should have less than a 5% chance of being false
131 hydrometeor detections.

132

133 WMBL clouds are isolated using the CPR_Echo_Top mask; Profile with high clouds (mask value 2), mid-level clouds
134 (mask value 3) and multi-layer clouds (mask value 5) are filtered out leaving low-level clouds, clear, and undetermined
135 profiles (mask values 4, 1 and 0 respectively; Fig. 1b). We additionally filter out profiles that have their maximum
136 reflectivity more than 150 m away from 0 m height; this last step is intended to identify profiles for which the CloudSat-



137 CPR was mispointing, which leads to vertical offset in the surface peak return.

138

139 **2.2 ARM Ground-based Observations**

140

141 The ARM program's KAZR is a 34.86 GHz (i.e., Ka-band) radar able of generating a 4 microsecond long symmetrical
142 vertical pulse creating a 0.3° wide 3-dB beamwidth. Following signal integration (1-s, 6,000-pulses), this radar
143 achieves a -44 dBZ minimum detectable signal (MDS) at 1 km. The KAZR is able to collect observations from 87 m
144 above ground to 18 km at ~ 30 m vertical resolution and 2 s time resolution [Lamer *et al.*, 2019]. Because the KAZR's
145 observations are not oversampled in the vertical, they are considered more independent than that of the CloudSat-
146 CPR.

147

148 We analyze the complete data record collected by the ground-based ARM sensors between October 2015 and
149 November 2017 (719 days) to 1) characterize the properties of WMBL clouds and precipitation (results in Sect. 4.0)
150 and 2) to evaluate the performance of theoretical radar architectures in detecting those clouds (results in Sect. 5.0).
151 This period also includes the 117 CloudSat overpass days, which we analyze separately to identify gaps specific to
152 the currently deployed CloudSat-CPR (results in Sect. 3.0).

153

154 For each analysis, we extract several complementary datasets from the ARM archive: i) KAZR general mode
155 (processing level a1): reflectivity, snr_copol (co-polar signal to noise ratio), ii) ceilometer: first_cloud_base_height,
156 iii) Parsivel laser disdrometer: equivalent radar reflectivity, and iv) radiosonde: temperature.

157

158 KAZR signal-to-noise ratio measurements are used as input to the *Hildebrand and Sekhon* [1974] algorithm to
159 distinguish significant echoes (hydrometeors and clutter) from noise. Liquid cloud base height determination from
160 collocated ceilometer is used to isolate radar echoes associated with cloud (above the first liquid cloud base height)
161 and precipitation (below the first liquid cloud base height) and to filter out clutter in the subcloud layer. Clutter filtering
162 is based on the argument that precipitation falling from cloud base should be continuous, thus any echo in the subcloud
163 layer detached from the main echo is labelled as clutter and is filtered out. All echoes thinner than 90m (3 range gates)
164 are also labelled as clutter and filtered out; comparison with the ceilometer confirms that this step does lead to the
165 removal of cloudy echoes. An example of processed radar reflectivity from KAZR is depicted in Fig. 1a.

166

167 Filtered KAZR radar reflectivity measurements are corrected for gas attenuation following *Rosenkranz* [1998] and
168 calibrated using observations collected during light precipitation events by the collocated surface-based Parsivel laser
169 disdrometer as well as using observations from the CloudSat-CPR collected over a small radius around the site
170 following *Kollias et al.* [2019].

171

172 WMBL cloud profiles are isolated from ice and high cloud containing profiles using KAZR radar reflectivity and
173 sonde temperature information. Only profiles having echoes below 5.5 km or below the height of the 0°C isotherm,
174 whichever one is lowest, are considered in this analysis.



175 2.3 Forward-simulations based on ground-based KAZR observations

176

177 Forward simulations are conducted to improve our understanding the CloudSat-CPR limitations and to identify
178 possible modifications which could lead to improvements in the detection of WMBL clouds (results in Sect. 5.0). We
179 forward simulate seven radar architectures. The first four are based on the CloudSat-CPR's current configuration
180 gradually improving each of its capabilities until it matches the configuration of the EarthCARE-CPR. The
181 EarthCARE-CPR design includes several improvements over CloudSat, namely:

182

- 183 1) a new asymmetrical point target response,
- 184 2) enhanced sensitivity,
- 185 3) a smaller field of view and integration distance, and
- 186 4) increased range oversampling.

187 The EarthCARE-CPR will also be the first spaceborne atmospheric radar capable of documenting the movement of
188 hydrometeors. This capability has been evaluated in several publications such as *Schutgens* [2008], *Battaglia et al.*
189 [2013], *Kollias et al.* [2014], *Sy et al.* [2014], and *Burns et al.* [2016] and is beyond the scope of this study. The last
190 two architectures are based on propositions made in the context of the National Aeronautics and Space Administration
191 (NASA)'s future Aerosol and Cloud, Convection and Precipitation (ACCP) mission ([https://science.nasa.gov/earth-](https://science.nasa.gov/earth-science/decadal-accp)
192 [science/decadal-accp](https://science.nasa.gov/earth-science/decadal-accp)). They both have:

193

- 194 1) increased range resolution but,
- 195 2) reduced sensitivity

196 Specifications for each radar configuration are given in Table 1 and Fig. 2.

197 Processed (i.e., filtered, corrected and calibrated) KAZR radar reflectivity observations (time-height) are used as input
198 to the forward-simulations. First, assuming a constant horizontal wind speed of 10 m s^{-1} , the KAZR time axis is
199 converted to horizontal distance. Then, to emulate the surface reflectivity which is not seen by KAZR, an artificial
200 surface echo is added to the processed KAZR reflectivity field at 0 m altitude (see Appendix I for more information
201 on how real CloudSat-CPR observations were used to construct this surface echo). Each spaceborne radar
202 configuration is simulated by first horizontally convolving the high-resolution (30 m x 20 m) KAZR reflectivity fields
203 using an along-track weighting function represented using a symmetrical gaussian distribution covering a distance
204 equivalent to 2 times the along-track field of view and then by vertically convolving the horizontally convolved
205 reflectivity field using either of the two range-weighting functions depicted in Fig. 2. The asymmetrical range
206 weighting function is modelled after that of the EarthCARE-CPR which was obtained from prelaunch testing of the
207 EarthCARE-CPR (provided by the mission's engineering team). The symmetrical range-weighting function used
208 (only) for the CloudSat_r forward simulation is modelled using a gaussian distribution adjusted to produce a surface



209 clutter echo profile similar to that observed by the CloudSat-CPR post-launch (more information in Appendix I).
210 Finally, along-track integration is emulated by averaging the convolved profiles in sections dictated by the integration
211 distance of each spaceborne radar without overlap between the section. Note that these forward-simulations are two
212 dimensional and as such do not capture cross-track effects; Also note that liquid attenuation and noise are not
213 represented.

214 For cloud and precipitation characterization, the forward-simulated radar reflectivity fields are finally filtered for
215 surface clutter. To do this, forward simulations of clear sky conditions are used to estimate the vertical extent and
216 intensity of surface clutter. For each radar configuration, for all heights affected by surface clutter, the clear sky surface
217 clutter reflectivity is removed from the forward-simulated radar reflectivity and only echoes with reflectivity at least
218 3 dB above the surface clutter reflectivity are conserved and deemed reliable. Otherwise, for all heights above the
219 surface clutter, only those echoes with reflectivity below the radar MDS are filtered out.

220

221 **2.4 Evaluation metrics**

222

223 Radars alone do not have the capability to distinguish between clouds and precipitation. For this reason, we often refer
224 to them as hydrometeor layers. The current study aims at characterizing:

225

226 i) the base of the lowest hydrometeor layer (cloud or virga base being indistinguishable), which we take to
227 be the height of the lowest radar echo in the profile;

228 ii) the top of the highest hydrometeor layer (i.e. cloud top), which we take to be the height of the highest
229 radar echo in the profile;

230 iii) the depth covered by hydrometeor layers, which we estimate as the distance between the top of the
231 highest hydrometeor layer and the base of the lowest hydrometeor layer.

232 Note that we report hydrometeor boundary heights at the center point of each radar's vertical range gate and not as its
233 upper or lower limit. This distinction, while seemingly insignificant for radars operating at a fine range sampling (e.g.,
234 KAZR 30 m), can become important for radar systems having a coarse range sampling (e.g., the CloudSat-CPR 240
235 m).

236

237 We also estimate over the entire observation periods:

238

239 i) hydrometeor cover, defined as the sum of all profiles containing at least one boundary-layer hydrometeor
240 echo divided by the total number of observed profiles (excluding those determined to contain high, deep
241 or ice clouds);

242 ii) the hydrometeor fraction profile, which we take is the number of boundary-layer hydrometeor echo at
243 each height divided by the total number of observed profiles (excluding those determined to contain
244 high, deep or ice clouds).



245 **3 Gaps**

246

247 Figure 1 illustrates examples of observations collected on Feb 27, 2016 near the ENA observatory. The ground-based
248 KAZR radar and ceilometer detected the presence of a thin (up to ~270 m) cloud layer whose properties varied
249 throughout the day. Between 0:00 and 10:00, cloud top height was observed to rise at a rate of roughly 21m hr⁻¹.
250 Shortly after 10:00, the KAZR detected signs of drizzle below the ceilometer-detected cloud base height at 941 m.
251 The vertical extent of this drizzle was observed to increase over the course of the day, until it eventually reached 87
252 m altitude (the lowest altitude at which KAZR measures) around 20:00. Besides changes in cloud top and hydrometeor
253 layer base height, the KAZR also measured changes in the radar reflectivity over the course of the day with more
254 intense radar reflectivity recorded coincidentally with deeper drizzle shafts.

255

256 At 15:05, CloudSat overpassed within 200 km of the KAZR and ceilometer location. Although the subset of noise-
257 and-clutter-filtered CloudSat-CPR observations show the presence of a hydrometeor layer, the hydrometeor layer
258 detected by the CloudSat-CPR had both breaks, a higher top (1.28 vs. 1.07 km) and a higher base (1.15 vs. 0.51 km)
259 than that detected by KAZR misleadingly making it appear thinner overall (Fig. 1b).

260

261 To illustrate how the aforementioned example is representative of the general picture of the WMBL cloud regimes at
262 the ENA, we also compared statistics of hydrometeor layer properties estimated for 89 of the 117 days where CloudSat
263 overpassed within 200 km of the ENA and boundary-layer clouds were the dominant cloud type (Fig. 3 and 4). For
264 this comparison, only KAZR and ceilometer observations taken within 4 hrs of the overpass are considered.

265

266 First, agreement between the KAZR reported cloud cover and the ceilometer reported cloud cover confirms that the
267 KAZR's sensitivity is sufficient to detect even the most tenuous clouds forming in this marine boundary layer regime;
268 this makes the KAZR an ideal sensor to document the properties of WMBL clouds and evaluate the CloudSat-CPR's
269 performance (Fig. 3a). Although not expected to perfectly match, the large hydrometeor cover discrepancy between
270 the KAZR (46.7%) and CloudSat-CPR (27.4%) suggest that the CloudSat-CPR fails to detect clouds in more than a
271 few (on the order of ~40%) of the atmospheric columns it samples (Fig. 3a). On the other hand, the CloudSat-CPR
272 seems to capture the shape and magnitude of the hydrometeor fraction profile above 1.0 km reasonably well (Fig. 3b).

273 This suggests that the CloudSat-CPR is able to detect the bulk of the thick hydrometeor layers controlling hydrometeor
274 fraction above 1.0 km. This also leads us to believe that the CloudSat-CPR's hydrometeor cover biases results either
275 from its inability to detect clouds entirely located below 1.0 km and/or due to its inability to detect thin and narrow
276 hydrometeor layers that are negligible contributors to hydrometeor fraction. Detailed analysis of the location of
277 individual cloud tops show evidence supporting both of these postulations (Fig. 4a). Specifically: 1) The distribution
278 of KAZR-detected cloud top heights shows clouds below 0.6 which are undetected by the CloudSat-CPR. We estimate
279 that this near-surface cloud mode produces 7.5% of the total cloud cover and so its misdetection could explain nearly
280 half of the CloudSat-CPR hydrometeor cover bias. 2) The distribution of KAZR-detected cloud top heights also shows
281 the presence of cloud top modes near 1.1 and 2.1 km that are only partially detected by the CloudSat-CPR (Fig. 4a).



282 These elevated cloud tops modes are likely related to the several echo bases between 1.4 and 2.5 km that nearly all
283 went undetected by the CloudSat-CPR (Fig. 4b). A figure showing time-height observations from two additional
284 overpass days allows us to visualize that these layers are generally thin, weakly reflective, and broken (Fig. 4i and ii).
285 We speculate that misdetection of such thin/tenuous clouds explains the remaining of the CloudSat-CPR's cloud cover
286 bias.

287

288 Beyond its inability to detect all cloudy columns, the CloudSat-CPR also severely underestimates the presence of
289 hydrometeors below 0.75 km because it suffers from surface echo contamination; this creates an artificial enhancement
290 in the number of apparent hydrometeor layer bases estimated from the CloudSat-CPR near 0.75 km and is not
291 representative of the true height of the base of either clouds or virga (Fig. 4b). We believe that the surface echo limits
292 the CloudSat-CPR's ability to observed true cloud base in approximately 52% of the cloudy columns it detects and
293 true virga base in ~80%; in other words, the CloudSat-CPR often provides an incomplete view of even the WMBL
294 cloud systems it does detect. This approximation is made based on the subset of cloudy columns observed by the
295 KAZR whose top is above the CloudSat-CPR surface clutter echo (1.0 km), and that are likely of sufficient thickness
296 (250 m) and reflectivity ($Z > -28$ dBZ) to be detected by the CloudSat-CPR.

297

298 **4 Challenges**

299

300 Although these 89 CloudSat overpasses are reasonably representative of the properties of the WMBL hydrometeor
301 systems found in the vicinity of the eastern north Atlantic facility, considering the entire set of measurements collected
302 by KAZR between October 2015 and November 2017 (719 days) provides additional insight on the challenges
303 associated with measuring the properties of these hydrometeor systems (Fig. 5).

304

305 Analysis of the ground-based observations suggests that WMBL cloud fraction exceeds 5% at all heights between 320
306 m and 2.09 km with cloud fraction peaking at 1.13 km (Fig. 5a; solid black curve). On the other hand, rain tends to be
307 found in the sub cloud layer below 1.28 km altitude occupying the largest fractional area between 100 m and 1.1 km
308 (Fig. 5a; dotted black curve). The low height at which WMBL clouds and precipitation are found is especially
309 challenging for spaceborne system which are known to suffer from contamination from the surface return. We estimate
310 that roughly 20% of the cloud echoes and 52% of the rain echoes recorded by the KAZR fall within the CloudSat-
311 CPR's surface echo region which extends at best only to 0.75 km (Fig. 5a; red curves).

312

313 The intensity (in terms of radar reflectivity) of cloud and precipitation also largely affects their ability to be detected
314 by radars. Using KAZR observations, we characterized the intensity of the hydrometeor echoes observed at each
315 height and report in Fig. 5b (colormap) the fraction of echoes with a reflectivity above a given threshold at each height.
316 Generally, cloud and precipitation producing radar reflectivity above a radar MDS can be detected. Thus, we would
317 expect that the CloudSat-CPR, with its -27dBZ MDS (depicted by the broken black line on Fig. 5b), should have the
318 capability to detect at best 80% of all cloud and/or echoes forming at any given height, de facto missing at least 20%



319 of hydrometeor echoes. Radar performance degrades within the surface clutter region. In the clutter region, only those
320 hydrometeor echoes whose intensity is larger than the surface echo intensity can be detected. To reflect this and for
321 reference, we overlaid on Fig. 5b the median reflectivity recorded by the CloudSat-CPR in clear sky days between
322 2010 and 2016 as well as its variability as quantified by the interquartile range (broken and dashed black lines
323 respectively). Over that time interval, the CloudSat-CPR's median surface echo varied from 37 dBZ at the surface
324 decreasing to -27 dBZ at 0.75km. Using this curve, we estimate that at 0.5 km height, based simply on sensitivity, the
325 CloudSat-CPR would miss at least 80% of the echoes detected by KAZR because their reflectivity is below that of the
326 surface clutter.

327

328 Adding to the challenge is the fact that boundary layer systems are shallow. Based on KAZR observations, 53% of
329 WMBL systems (cloud and rain) forming at ENA are shallower than 500 m, 33% shallower than 250 m and 16%
330 shallower than 100 m (Fig. 5c; red line). Sampling hydrometeor layers using radar pulses longer than the hydrometeor
331 layer thickness inherently produces partial beam filling issues, which lead to a weakening of the returned power. This
332 results in an underestimation of the reflectivity of the thin echoes sampled and may even lead to their misdetection if
333 the resulting reflectivity is below the radar MDS. There is also an unfortunate relationship between hydrometeor layer
334 thickness and mean reflectivity such that thin layers not only suffer from more partial beam filling, but also have
335 weaker reflectivities. The black curve on Fig. 5c shows the median hydrometeor layer mean reflectivity as a function
336 of hydrometeor layer thickness. From this figure we can estimate that 500 m layer thick hydrometeor layers typically
337 have a mean reflectivity of -21 dBZ, 250m thick layers -26 dBZ, 100m thick layers -33 dBZ.

338

339 **5 Path forward**

340

341 Improving our ability to detect boundary layer clouds and precipitation could likely be achieved through the following
342 radar system modifications including (not necessarily in order of importance):

343

- 344 1) Alter the range weighting function
- 345 2) Decrease the minimum detectable signal (MDS)
- 346 3) Reduce the horizontal field of view
- 347 4) Increase the vertical sampling
- 348 5) Reduce the transmitted pulse length.

349 We emulate the impact of these radar modifications by constructing forward-simulations for 7 radar configurations,
350 each of which has been gradually improved by the aforementioned radar modification (described in Sect. 2.3, Table 1
351 and Fig. 2). Quantitative assessment of the performance of the forward-simulated radar configurations is estimated
352 based on a set of 719 forward-simulations constructed from KAZR observations collected between October 2015 and
353 November 2017. Like done for the real CloudSat-CPR observations in Sect. 3.0, performance is evaluated in terms of
354 how well hydrometeor cover and hydrometeor fraction are captured (Fig. 7) as well as how accurately the boundaries



355 of hydrometeor layers are detected (Fig. 8). However, since all forward simulations presented in this section are based
356 on the same KAZR observations, we expect a perfect match and interpret any deviations from the KAZR observations
357 as a bias. To help visualize the performance of the 7 radar configurations, we present output from forward-simulations
358 of the February 27, 2016 hydrometeor layer. The KAZR's view of this hydrometeor layer was depicted and described
359 in Fig. 1a and Sect. 3.0; for reference the KAZR's detected echo top and base are overlaid on each forward-simulation
360 in Fig. 6 using black dots.

361

362 First, we validate our forward simulation framework by simulating the CloudSat-CPR's current configuration (results
363 depicted in royal blue and designated as CloudSat_f for short). CloudSat_f's forward simulations show similar biases
364 than the real CloudSat-CPR when compared to KAZR indicating that the forward simulator captures enough of the
365 radars characteristics to reasonably emulate its performance. In a nutshell, the CloudSat_f underestimates hydrometeor
366 cover by more than 10% (Fig. 7a) likely owing to its misdetection of an important fraction of clouds with tops between
367 750 m and 1.75 km (Fig. 8a) and its inability to detect the small fraction of clouds forming entirely below 500 m. Just
368 like the real CloudSat-CPR, the CloudSat_f performs well in capturing hydrometeor fraction between 750 m and 3 km
369 but poorly below that height since it suffers from contamination by surface clutter (Fig. 7b).

370

371 Prelaunch testing of the EarthCARE-CPR showed that its pulse generates an asymmetrical point target response. This
372 mean that, unlike the CloudSat-CPR, the EarthCARE-CPR has an asymmetrical range weighting function (Fig. 2).
373 The range weighting function of the EarthCARE-CPR's pulse has a rapid cut off at a factor of 0.5 time the pulse length
374 at its leading edge, and a longer taper extending off to 1.5 times the pulse at its trailing edge. To isolate performance
375 changes resulting strictly from this range weighting function, we contrast the result of *forward* simulations performed
376 with the CloudSat-CPR's original configuration (CloudSat_f results depicted in royal blue) and with a CloudSat-like
377 configuration with the EarthCARE-CPR's *asymmetrical* range weighting function (CloudSat_a, results depicted in
378 cyan). Time-series comparison of CloudSat_a (Fig. 6b) and CloudSat_f (Fig. 6a) reflectivity shows that the asymmetrical
379 range weighting function reduces the vertical extent of the surface clutter echo, allowing for the detection of a larger
380 fraction of hydrometeor at 500 m. Over the entire set of 719 forward simulations, this leads to improvements in the
381 representation of the hydrometeor fraction profile (Fig. 7b) and of the echo base height distribution (not shown) around
382 500 m. However, differences in the echo base height from KAZR (black dots) and from CloudSat_a (cyan dots) suggest
383 that changes in the shape of the pulse point target response alone are insufficient to accurately detect the base of the
384 precipitating WMBL systems found at the ENA (Fig. 6b). We also note that the change in range weighting function
385 shape alone only marginally improve CloudSat_f's ability to determine hydrometeor cover (improvement from 27.9%
386 to 28.2% compared to 39.1% reported by KAZR); The reason for this is that hydrometeor cover is controlled by thin,
387 tenuous clouds and clouds located entirely below 0.5 km. As a potential drawback, the asymmetrical range weighting
388 function seems to lead to slightly more vertical stretching of cloud top signals (on average 37 m) such as visible by
389 comparing the examples in Fig. 6a and 6b, and in Fig. 8a. When compounded over the entire ensemble of forward
390 simulated clouds this leads to a 0.24% overestimation of hydrometeor fraction at all height between 0.75 and 3.00 km
391 (Fig. 7b). The vertical stretching of cloud tops results from the rapid taper of the pulse between a factor of -0.5-0.0 of



392 the pulse lengths which is accompanied by additional power being focused in that region of the pulse in contrast to a
393 symmetrical pulse such as that of the CloudSat-CPR (see Fig. 2).

394

395 Besides having an asymmetrical range weighting function, the EarthCARE-CPR will also operate with a MDS of -35
396 dBZ which is 7 dB more sensitive than the CloudSat-CPR. To isolate performance changes resulting strictly from this
397 sensitivity enhancement, we contrast the result of forward simulations performed with a CloudSat-like configuration
398 with the *asymmetrical* range weighting functions (CloudSat_a, results depicted in cyan) with that of a CloudSat-like
399 configuration with both an *asymmetrical* range weighting function *and enhanced sensitivity* (CloudSat_{a+es}, results
400 depicted in purple). Time-series comparison of CloudSat_{a+es} (Fig. 6d) and CloudSat_a (Fig. 6b) reflectivity shows that
401 the sensitivity enhancement allows for the detection of hydrometeors in previously undetected columns such as the
402 broken hydrometeor segments observed by KAZR around 100 km distance along the forward-simulated track.
403 Quantitatively, the more sensitive CloudSat-CPR configuration detects 8% more cloudy columns than either of the
404 other two CloudSat-CPR configurations discussed so far (i.e., with or without the asymmetrical range weighting
405 function) missing only 2.4% of the cloudy columns detected by KAZR (Fig. 7a). This implies that, if an important
406 mission objective is detecting even tenuous cloudy columns, improving the MDS is crucial. That being said, we advise
407 against accomplishing this by transmitting a longer pulse (e.g., like done in the first 4 years of operation of the GPM-
408 CPR) since there are two main drawbacks to transmitting a long pulse with a higher sensitivity, both caused by partial
409 beam filling. Firstly, the enhanced sensitivity leads to additional vertical stretching of cloud boundaries, an effect
410 visible between 400 and 800 km along track when comparing Fig. 6d to 6b. This is because the signal from cloud
411 boundaries away from their location resulting from their interaction with the edges of the radar range weighting
412 function now exceeds the MDS. Secondly, the enhanced sensitivity also leads to previously undetected thin layers
413 becoming detectable, but it stretches them vertically at least to the vertical extent of the radar pulse length. From
414 changes in the location of the cloud top height distribution peak shown in Fig. 8a, we estimate that enhancing the
415 sensitivity of a 3.3 microsecond long pulse from -28 dBZ to -35dBZ would lead to a 250 m bias in detected cloud top
416 height for the types WMBL clouds forming at the ENA. Moreover, because it both vertically stretches clouds and
417 detects more real clouds, the highly sensitive CloudSat_{a+es} overestimates hydrometeor cover by up to 7% at all heights
418 between 500 m and 3.0 km (Fig. 7b).

419

420 Since EarthCARE will travel at an altitude closer to the Earth surface it will also have half the horizontal field of view
421 of CloudSat. Our results suggest that halving the CloudSat-CPR's horizontal field of view and halving its integration
422 distance would lead to a slight reduction in its estimated hydrometeor cover (1.7% less). We take this as an indication
423 that the larger horizontal field of view of the CloudSat-CPR only marginally artificially broadens broken clouds (see
424 CloudSat_{a+es+hf}, results depicted in gold in Fig. 7). That being said, note that this result, like all the others presented
425 here, is based on 2-D forward-simulation and as such it does not take into account cross-track effects which may also
426 generate biases especially in sparse broken cloud fields.

427

428 Another interesting radar configuration proposed by the EarthCARE mission advisory group concerns the amount of



429 vertical oversampling of the radar pulse. Radar signals are typically oversampled by a factor of two effectively halving
430 the vertical spacing between available measurements. The EarthCARE-CPR will use a factor of 5 oversampling to
431 increase its vertical range sampling to 100 m while still operating at a 500 m vertical resolution. While oversampling
432 may be appealing because it creates a smoother view of cloud fields, it does not effectively improve the vertical
433 resolution because of the correlations between the oversampled measurements. Evaluating the impact of these
434 correlations on the observed radar reflectivity field is beyond the scope of this study which instead focuses on
435 evaluating the impact of oversampling on accurately locating cloud and precipitation boundaries. Time-series of
436 EarthCARE (Fig. 6b) reflectivity shows that increased oversampling will allow for a more precise characterization
437 of the variability of echo base and top height (also see the echo top height distribution presented in Fig. 8c).
438 Comparison of the ensemble of EarthCARE (magenta) and CloudSat_{+es+hf} (gold) forward-simulations indicates that
439 this precision can be achieved without causing significant biases in hydrometeor cover (Fig. 7a) or hydrometeor
440 fraction (Fig. 7c).

441

442 Although the EarthCARE-CPR's performance is significantly better than that of the CloudSat-CPR when it comes to
443 detecting thin, tenuous and broken clouds as well as clouds and precipitation near 500 m, its configuration still does
444 not allow to detect all WMBL clouds and precipitation. Remaining detection limitations occur below 500 m within
445 the region of the surface clutter echo. Additional reduction of the vertical extent of the surface clutter can be achieved
446 by reducing the pulse length. This, however, comes at the expense of reduced sensitivity. Comparing EarthCARE
447 (results depicted in magenta), ACCP₂₅₀ (results depicted in red) and ACCP₁₀₀ (results depicted in green) simulations
448 allows us to see the gain and penalty incurred from shortening the radar vertical range resolution from 500 m, to 250
449 m to 100 m at the cost of reducing sensitivity from -35 dBZ to -26 dBZ and -17dBZ. In alignment with our previous
450 conclusion that a high sensitivity is necessary for detecting all cloudy columns, reducing the radar pulse length and
451 sensitivity reduces the fraction of cloudy columns which can be detected by the ACCP configurations (Fig. 7a). For
452 instance, the ACCP₂₅₀ configuration, which is nearly as sensitive as CloudSat (-26 dB versus -28 dB), performs very
453 similarly in terms of the number of cloudy columns it is able to detect (Fig. 7a) and in terms of how well it can capture
454 the vertical distribution of hydrometeors between 500 m and 3.0 km (Fig. 7d) which we determined is influenced by
455 the deeper more reflective clouds rather than the thin and tenuous ones. The ACCP₂₅₀ configuration does, however,
456 have the advantage of providing information on the base of clouds and/or precipitation down to 250 m which is much
457 more than the CloudSat-CPR can achieve (Fig. 7d). ACCP₂₅₀'s shorter pulse also helps mitigate the amount of cloud
458 stretching related to partial beam filling issues thus providing a more precise characterization of cloud top height (Fig.
459 8c, effects also visible in Fig. 6e). So generally speaking, reducing vertical pulse length reduces the fraction of detected
460 cloudy columns but improves the characterization (both in terms of echo top and echo base location) of those cloudy
461 columns which are detected.

462

463 Results also suggest that radars with shorter less sensitive pulses would be more suitable for the characterization of
464 surface rain and virga, which are more reflective targets. In fact, we estimate that ACCP₁₀₀ would detect 18% out of
465 the 26% rainy columns detected by the KAZR (Fig. 7a). ACCP₁₀₀ would also do reasonably well at capturing the



466 vertical distribution of drizzle and rain; comparisons of rain fraction profiles estimated from the KAZR (subcloud
467 layer only) suggest that ACCP₁₀₀ would miss < 2% of the virga forming at each height below 750 m and would be
468 able to detect the presence of rain as close as 25 m from the surface.

469

470 **6 Discussion and conclusions**

471

472 The macrophysical properties of warm marine boundary layer (WMBL) clouds and precipitation and spaceborne
473 radars ability to characterize them is evaluated using ground-based ceilometer and Ka-band ARM Zenith Radar
474 (KAZR) observations collected over the Atmospheric Radiation Measurement (ARM) program Eastern North Atlantic
475 (ENA) facility.

476

477 Analysis of 719 days of KAZR observations collected between October 2015 and November 2017 suggest that the
478 following three main properties of WMBL clouds and precipitation complicate their detection by spaceborne radars:

479

480 1) They are generally thin, with 50 % of the hydrometeors layer detected by KAZR having a thickness below
481 400 m. As a result, they may not fill the entire spaceborne radar pulse volumes causing serious partial beam
482 filling issues.

483 2) They are weakly reflective, with 50 % of the hydrometeors detected by KAZR having reflectivity below -22
484 dBZ. We also find that hydrometeor layer mean reflectivity is strongly related to hydrometeor layer thickness
485 such than the thinnest layers are also typically the least reflective ones, further challenging their detection.

486 3) They form at low levels, with 50% of WMBL cloud echoes being located below 1.2 km and 50 % of sub-
487 cloud layer rain echoes below 0.75 km. Therefore, their backscattered power may easily overlap and be
488 masked by the strong surface return detected by spaceborne radars.

489 Observations from 89 daytime overpasses and results from 719 2-D forward simulations constructed using KAZR
490 observations consistently shows that the CloudSat-CPR fails to detect 29-41% of the cloudy columns detected by the
491 ground based KAZR. Supporting the postulations of both *Christensen et al.* [2013], *Rapp et al.* [2013] and *Liu et al.*
492 [2018], our results suggest that a little over half of this bias can be attributed to the CloudSat-CPR inability to sample
493 thin, tenuous cloud while the other half results from misdetection of clouds that form entirely within the CloudSat-
494 CPR surface (some of which are also thin and tenuous). Using forward simulations, we determined that mitigating the
495 vertical extent of the surface clutter by changing its range weighing function or by reducing its vertical range resolution
496 by half would only partially improve the CloudSat-CPR's ability to detect all cloudy columns, which is very much
497 limited by the CloudSat-CPR's low sensitivity. In other words, when it comes to detecting all cloudy columns, we
498 find that improving radar MDS is more important than reducing the vertical extent of the surface clutter. For this
499 reason, the 7 dB more sensitive EarthCARE-CPR is expected to detect significantly (19.7%) more cloudy columns
500 than the CloudSat-CPR, only missing < 9.0% of the simulated cloudy columns.

501



502 On the other hand, our overpass and forward-simulation results also suggest that the CloudSat-CPR is able to capture
503 the general vertical distribution of hydrometeor (i.e., hydrometeor fraction profile) above 750 m which we find is
504 dominantly controlled by thicker more reflective clouds. Unfortunately, we estimate that because of its asymmetrical
505 range weighting function and because of the long length of his highly sensitive pulse, the EarthCARE-CPR's will
506 overestimate (by ~250 m) cloud top height and underestimate cloud base height, making hydrometeor layers appear
507 artificially thicker than they are, which will also bias the EarthCARE-CPR's hydrometeor fraction estimates. This
508 effect would need to be addressed to extract accurate information about the location of cloud boundaries and about
509 the vertical distribution of clouds and precipitation, two aspects likely to become increasingly important as we continue
510 moving towards increasingly high-resolution global modeling. Synergy with a collocated ceilometer could potentially
511 help correct cloud top height, however, such corrections would only be possible in single layer conditions and
512 alternative techniques would need to be developed to improve the EarthCARE-CPR's ability to accurately estimate
513 the vertical extent of multi-layer boundary layer clouds.

514

515 Below 1.0 km, the surface clutter echo seen by the CloudSat-CPR masks portions of clouds and virga. Based on a
516 subset of KAZR observations, we estimate that the surface echo limits the CloudSat-CPR's ability to observed true
517 cloud base in ~52% of the cloudy columns it detects and true virga base in ~80%. In other words, the CloudSat-CPR
518 often provides an incomplete view of even these cloud systems it does detect. Our analysis of real CloudSat-CPR's
519 observations shows that the clutter mask part of the GEOPROF version 4.0 product is relatively aggressive, and we
520 believe the CloudSat-CPR's performance could perhaps be somewhat improved by revising this clutter mask. In terms
521 of future spaceborne radar missions, radar architectures with finer range resolution could more precisely characterize
522 the boundaries of hydrometeor layers. For instance, the 250-m range resolution (oversampled at 125-m) radar
523 architecture presented here produces echo top height statistics comparable to that of the ground based KAZR in terms
524 of detecting the minimum, maximum and mode of the distributions. However, since a shorter pulse can currently only
525 be achieved at the expense of reduced sensitivity, this radar would suffer from the limitations similar to that of the
526 CloudSat-CPR in terms of the number of cloudy columns it could detect. This means that while improving the
527 detection of virga below 500 m might be possible, improving the detection of cloud bases below 500 m is unlikely
528 achievable with current technologies.

529

530 Overall this analysis suggests that no one single radar configuration can adequately detect all WMBL clouds while
531 simultaneously accurately determining the height of cloud top, cloud base and virga base. The alternative of deploying
532 spaceborne radars capable of operating with interlaced operation modes is thus worth considering [Kollias *et al.*,
533 2007]. For example, a radar capable of generating both a highly sensitive long-pulse mode and a less sensitive but
534 clutter limiting short-pulse mode would likely provide a more comprehensive characterization of the boundary layer
535 by detecting both low-reflectivity clouds and low-altitude rain.

536

537 On a related note, it is likely that the partial beam filling issues identified here as affecting both the CloudSat-CPR
538 and the EarthCARE-CPR ability to locate clouds might, as hinted by Burns *et al.* [2016], also affect their ability to



539 accurately measure their true reflectivity. Such radar reflectivity biases would affect water mass retrievals performed
540 using radar reflectivity measurement and follow up efforts should aim at quantifying this effect and should look into
541 alternative retrieval techniques and/or radar configurations that could address this issue [Battaglia *et al.*, In
542 preparation].

543

544 As a final thought we also point out that, due to the variations in the microphysical and macrophysical properties of
545 oceanic warm clouds globally, the actual missed detections by the various spaceborne-CPR architectures described
546 here may change when considering other regimes. Liu *et al.* [2016] study hints at the fact that regions dominated by
547 stratiform clouds are more challenging to characterize than those dominated by cumulus. Thus, for completeness,
548 follow on studies could test the performance of the radar configurations proposed here in other climatic regimes.

549

550 **Authors contributions**

551

552 K. Lamer coordinated the project, extracted the ground-based measurement files from the ARM archive, performed
553 the data analysis and produced the final manuscript draft. P. Kollias extracted the CloudSat-CPR GEOPROF product
554 files from the data processing center and provided feedback on the forward-simulator. A. Battaglia provided feedback
555 on the analysis methods as well as on the manuscript draft. S. Preval performed exploratory data analysis and provided
556 feedback on the manuscript draft.

557

558 **Acknowledgements**

559

560 K. Lamer's contributions were supported by U.S. Department of Energy Atmospheric System Research project DE-
561 SC0016344. P. Kollias's contributions were supported by the U.S. Department of Energy Atmospheric Systems
562 Research program and the ENA site scientist award. A. Battaglia and S. Preval's contributions were supported by the
563 U.S. Department of Energy Atmospheric System Research project DE-SC0017967.

564

565 **Data Availability**

566

567 All CloudSat-CPR observations were obtained from the CloudSat data processing center ([www.
568 http://www.cloudsat.cira.colostate.edu/](http://www.cloudsat.cira.colostate.edu/)). All ARM observations were obtained from the ARM archive
569 (<https://www.archive.arm.gov/discovery/>). Output of all forward-simulations is fully reproducible from the
570 information given.

571

572

573

574

575

576



577 **Appendix I**

578

579 Since the Earth surface can be treated as a point target, observations of the surface clutter echo during clear sky
580 conditions can be used to gain insight into how the energy contained within radar pulse spreads out vertically when it
581 hits a point target (i.e. about range-weighting function).

582

583 We extract information about the shape of the CloudSat-CPR's range-weighting function from a subset of observations
584 collected between May 2010 and November 2017 identified as clear sky in the GEOPROF product (version 4.0;
585 CPR_Echo_Top mask variable). We further ignore observations from non-significant echoes ($Z < -27$ dBZ) and
586 mispointing events (profiles, which have their maximum reflectivity more than 75 m from 0 m height). Over this
587 period, the median surface reflectivity profile (depicted by the broken black profile in Fig. 5c) shows a main peak at
588 surface level quickly reducing in intensity within height; the surface radar reflectivity return was observed to reduce
589 by ~ 34 dB at a distance of 0.5 km (i.e., half the pulse length) away from its actual location at the surface. A secondary
590 lobe whose peak intensity is ~ 50 dB lower than that of the main lobe was observed to spread from a distance of roughly
591 0.5 km to 1.0 km away from the main peak. Characterization of the CloudSat-CPR point-target response presented in
592 *Tanelli et al.* [2008] also revealed the symmetrical character of the main lobe of the CloudSat-CPR range-weighting
593 function; the prelaunch analysis also showed that the presence of this secondary is confined to the pulse's leading
594 edge.

595

596 In the current analysis, we first use the median surface reflectivity profile we extracted (post-launch) to adjust the
597 width of the gaussian range weighting function used in the CloudSat forward-simulator. The gaussian range weighting
598 function depicted in Fig. 2 produces a forward-simulated surface echo return similar, in intensity and vertical extent,
599 to the surface echo observed by the CloudSat-CPR under clear sky conditions (compare the royal blue line and black
600 lines in Fig. 5b). Note that we did not attempt to reproduce the CloudSat-CPR's secondary lobe and that the use of
601 this gaussian range weighting function is limited to the CloudSat_r forward simulation. All other forward simulations
602 are conducted using the EarthCARE-CPR asymmetrical range weighting function constructed from pre-launch testing
603 of the EarthCARE-CPR.

604

605 The strength of the surface echo observed by CloudSat under clear sky conditions is also used to determine the
606 intensity of the surface clutter artificially input to the KAZR reflectivity field. We estimate the surface echo to be
607 added to KAZR's -30 m to 0 m range gate should have an intensity of 52 dBZ such that after its convolution by the
608 range weighting functions of the spaceborne radar configurations, the strength of the realized surface echo at 0 m
609 height is 41 dBZ matching the strength of the surface echo observed by CloudSat under clear sky conditions (depicted
610 by the broken black line in Fig. 5b). Note that variability of the surface return due to attenuation of the radar signal by
611 liquid, heterogeneous surface conditions, and changes in satellite altitude have not been included in the forward-
612 simulator. However, analysis of the real CloudSat surface echo observed during clear sky suggest that variability due
613 to heterogeneous surface conditions, and changes in satellite altitude are on the order of < 2 dB (depicted by the dotted
614 black lines in Fig. 5b).



615 **References**

616

- 617 Battaglia, A., et al. (Submitted), Space-borne cloud and precipitation radars: status, challenges and ways forward,
618 *Reviews of Geophysics*.
- 619 Battaglia, A., P. Kollias, K. Lamer, R. Dhillon, and D. Watters (In preparation), Mind-the-gap Part II: Towards
620 quantifying warm rain using spaceborne sensors.
- 621 Battaglia, A., S. Tanelli, and P. Kollias (2013), Polarization Diversity for Millimeter Spaceborne Doppler Radars:
622 An Answer for Observing Deep Convection?, *Journal of Atmospheric and Oceanic Technology*, 30(12),
623 2768-2787, doi:10.1175/jtech-d-13-00085.1.
- 624 Bony, S., B. Stevens, D. M. Frierson, C. Jakob, M. Kageyama, R. Pincus, T. G. Shepherd, S. C. Sherwood, A. P.
625 Siebesma, and A. H. Sobel (2015), Clouds, circulation and climate sensitivity, *Nature Geoscience*, 8(4),
626 261-268.
- 627 Bretherton, C. S., R. Wood, R. George, D. Leon, G. Allen, and X. Zheng (2010), Southeast Pacific stratocumulus
628 clouds, precipitation and boundary layer structure sampled along 20 S during VOCALS-REx, *Atmospheric*
629 *Chemistry and Physics*, 10(21), 10639-10654.
- 630 Burleyson, C. D., S. P. De Szoeke, S. E. Yuter, M. Wilbanks, and W. A. Brewer (2013), Ship-based observations of
631 the diurnal cycle of southeast Pacific marine stratocumulus clouds and precipitation, *Journal of the*
632 *Atmospheric Sciences*, 70(12), 3876-3894.
- 633 Burns, D., P. Kollias, A. Tatarevic, A. Battaglia, and S. Tanelli (2016), The performance of the EarthCARE Cloud
634 Profiling Radar in marine stratiform clouds, *Journal of Geophysical Research: Atmospheres*, 121(24).
- 635 Christensen, M. W., G. L. Stephens, and M. D. Lebsock (2013), Exposing biases in retrieved low cloud properties
636 from CloudSat: A guide for evaluating observations and climate data, *Journal of Geophysical Research:*
637 *Atmospheres*, 118(21), 12,120-112,131.
- 638 Comstock, K. K., C. S. Bretherton, and S. E. Yuter (2005), Mesoscale variability and drizzle in southeast Pacific
639 stratocumulus, *Journal of the Atmospheric Sciences*, 62(10), 3792-3807.
- 640 Dong, X., and G. G. Mace (2003), Arctic stratus cloud properties and radiative forcing derived from ground-based
641 data collected at Barrow, Alaska, *Journal of Climate*, 16(3), 445-461.
- 642 Ellis, T. D., T. L'Ecuyer, J. M. Haynes, and G. L. Stephens (2009), How often does it rain over the global oceans?
643 The perspective from CloudSat, *Geophysical Research Letters*, 36(3).
- 644 Frisch, A., C. Fairall, and J. Snider (1995), Measurement of stratus cloud and drizzle parameters in ASTEX with a
645 Ka-band Doppler radar and a microwave radiometer, *Journal of the Atmospheric Sciences*, 52(16), 2788-
646 2799.
- 647 Haynes, J. M., C. Jakob, W. B. Rossow, G. Tselioudis, and J. Brown (2011), Major characteristics of Southern
648 Ocean cloud regimes and their effects on the energy budget, *Journal of Climate*, 24(19), 5061-5080.
- 649 Hildebrand, P. H., and R. Sekhon (1974), Objective determination of the noise level in Doppler spectra, *Journal of*
650 *Applied Meteorology*, 13(7), 808-811.
- 651 Huang, Y., S. T. Siems, M. J. Manton, L. B. Hande, and J. M. Haynes (2012), The structure of low-altitude clouds



- 652 over the Southern Ocean as seen by CloudSat, *Journal of Climate*, 25(7), 2535-2546.
- 653 Illingworth, A. J., H. Barker, A. Beljaars, M. Ceccaldi, H. Chepfer, N. Clerbaux, J. Cole, J. Delanoë, C. Domenech,
654 and D. P. Donovan (2015), The EarthCARE satellite: The next step forward in global measurements of
655 clouds, aerosols, precipitation, and radiation, *Bulletin of the American Meteorological Society*, 96(8), 1311-
656 1332.
- 657 Klein, S. A., and D. L. Hartmann (1993), The seasonal cycle of low stratiform clouds, *Journal of Climate*, 6(8),
658 1587-1606.
- 659 Kollias, P., B. Puigdomènech Treserras, and A. Protat (2019), Calibration of the 2007–2017 record of Atmospheric
660 Radiation Measurements cloud radar observations using CloudSat, *Atmospheric Measurement Techniques*,
661 12(9), 4949-4964.
- 662 Kollias, P., W. Szyrmer, J. Rémillard, and E. Luke (2011), Cloud radar Doppler spectra in drizzling stratiform
663 clouds: 2. Observations and microphysical modeling of drizzle evolution, *Journal of Geophysical*
664 *Research: Atmospheres*, 116(D13).
- 665 Kollias, P., W. Szyrmer, I. Zawadzki, and P. Joe (2007), Considerations for spaceborne 94 GHz radar observations
666 of precipitation, *Geophysical Research Letters*, 34(21).
- 667 Kollias, P., S. Tanelli, A. Battaglia, and A. Tatarevic (2014), Evaluation of EarthCARE cloud profiling radar
668 Doppler velocity measurements in particle sedimentation regimes, *Journal of Atmospheric and Oceanic*
669 *Technology*, 31(2), 366-386.
- 670 Lamer, K., and P. Kollias (2015), Observations of fair-weather cumuli over land: Dynamical factors controlling
671 cloud size and cover, *Geophysical Research Letters*, 42(20), 8693-8701.
- 672 Lamer, K., P. Kollias, and L. Nuijens (2015), Observations of the variability of shallow trade wind cumulus
673 cloudiness and mass flux, *Journal of Geophysical Research: Atmospheres*, 120(12), 6161-6178.
- 674 Lamer, K., B. Puigdomènech Treserras, Z. Zhu, B. Isom, N. Bharadwaj, and P. Kollias (2019), Characterization of
675 shallow oceanic precipitation using profiling and scanning radar observations at the Eastern North Atlantic
676 ARM observatory, *Atmospheric Measurement Techniques*, 12(9), 4931-4947.
- 677 Leon, D. C., Z. Wang, and D. Liu (2008), Climatology of drizzle in marine boundary layer clouds based on 1 year of
678 data from CloudSat and Cloud-Aerosol Lidar and Infrared Pathfinder Satellite Observations (CALIPSO),
679 *Journal of Geophysical Research: Atmospheres*, 113(D8).
- 680 Liu, D., Q. Liu, G. Liu, J. Wei, S. Deng, and Y. Fu (2018), Multiple Factors Explaining the Deficiency of Cloud
681 Profiling Radar on Detecting Oceanic Warm Clouds, *Journal of Geophysical Research: Atmospheres*,
682 123(15), 8135-8158.
- 683 Liu, D., Q. Liu, L. Qi, and Y. Fu (2016), Oceanic single-layer warm clouds missed by the Cloud Profiling Radar as
684 inferred from MODIS and CALIOP measurements, *Journal of Geophysical Research: Atmospheres*,
685 121(21), 12,947-912,965.
- 686 Marchand, R., G. G. Mace, T. Ackerman, and G. Stephens (2008), Hydrometeor detection using CloudSat—An
687 Earth-orbiting 94-GHz cloud radar, *Journal of Atmospheric and Oceanic Technology*, 25(4), 519-533.
- 688 Nam, C., S. Bony, J. L. Dufresne, and H. Chepfer (2012), The ‘too few, too bright’ tropical low-cloud problem in



- 689 CMIP5 models, *Geophysical Research Letters*, 39(21).
690 Protat, A., D. Bouniol, J. Delanoë, E. O'Connor, P. May, A. Plana-Fattori, A. Hasson, U. Górsdorf, and A.
691 Heymsfield (2009), Assessment of CloudSat reflectivity measurements and ice cloud properties using
692 ground-based and airborne cloud radar observations, *Journal of Atmospheric and Oceanic Technology*,
693 26(9), 1717-1741.
694 Rapp, A. D., M. Lebsock, and T. L'Ecuyer (2013), Low cloud precipitation climatology in the southeastern Pacific
695 marine stratocumulus region using CloudSat, *Environmental Research Letters*, 8(1), 014027.
696 Rosenkranz, P. W. (1998), Water vapor microwave continuum absorption: A comparison of measurements and
697 models, *Radio Science*, 33(4), 919-928.
698 Sassen, K., and Z. Wang (2008), Classifying clouds around the globe with the CloudSat radar: 1-year of results,
699 *Geophysical Research Letters*, 35(4), doi:10.1029/2007gl032591.
700 Schutgens, N. (2008), Simulated Doppler radar observations of inhomogeneous clouds: Application to the
701 EarthCARE space mission, *Journal of atmospheric and oceanic technology*, 25(1), 26-42.
702 Sherwood, S. C., S. Bony, and J.-L. Dufresne (2014), Spread in model climate sensitivity traced to atmospheric
703 convective mixing, *Nature*, 505(7481), 37.
704 Stephens, G. L., D. G. Vane, R. J. Boain, G. G. Mace, K. Sassen, Z. Wang, A. J. Illingworth, E. J. O'Connor, W. B.
705 Rossow, and S. L. Durden (2002), The CloudSat mission and the A-Train: A new dimension of space-
706 based observations of clouds and precipitation, *Bulletin of the American Meteorological Society*, 83(12),
707 1771-1790.
708 Stephens, G. L., D. Winker, J. Pelon, C. Trepte, D. Vane, C. Yuhas, T. L'ecuyer, and M. Lebsock (2018), CloudSat
709 and CALIPSO within the A-Train: Ten years of actively observing the Earth system, *Bulletin of the*
710 *American Meteorological Society*, 99(3), 569-581.
711 Sy, O. O., S. Tanelli, P. Kollias, and Y. Ohno (2014), Application of matched statistical filters for EarthCARE cloud
712 Doppler products, *IEEE Transactions on Geoscience and Remote Sensing*, 52(11), 7297-7316.
713 Tanelli, S., S. L. Durden, E. Im, K. S. Pak, D. G. Reinke, P. Partain, J. M. Haynes, and R. T. Marchand (2008),
714 CloudSat's cloud profiling radar after two years in orbit: Performance, calibration, and processing, *IEEE*
715 *Transactions on Geoscience and Remote Sensing*, 46(11), 3560-3573.
716
717



718 **Tables**

719

720 **Table 1.** Specifications of the forward-simulated radar configurations including information about whether or not their
 721 pulse weighting function is symmetrical (sym.) or asymmetrical (asym.) in either the vertical or the along-track
 722 dimension.

723

Forward-simulated radar architectures	Sensitivity (dBZ)	Vertical dimension					Along-track dimension		
		Pulse length (km)	Range resolution 6-dB (m)	Oversampling	Range sampling (m)	Range weighting function shape	Instantaneous field of view (km)	Integration distance (km)	Weighting function shape
CloudSat _r	-28	1.0	500	2	250	Sym.*	1.4	1.0	Sym.
CloudSat _a	-28	1.0	500	2	250	Asym*	1.4	1.0	Sym.
CloudSat _{a+es}	-35	1.0	500	2	250	Asym*	1.4	1.0	Sym.
CloudSat _{a+es+hhf}	-35	1.0	500	2	250	Asym*	0.7	0.5	Sym.
EarthCARE	-35	1.0	500	5	100	Asym*	0.7	0.5	Sym.
ACCP ₂₅₀	-26	0.5	250	2	125	Asym*	0.7	0.5	Sym.
ACCP ₁₀₀	-17	0.2	100	2	50	Asym*	0.7	0.5	Sym.

724 * Shape of the range weighting function is depicted in Fig. 2

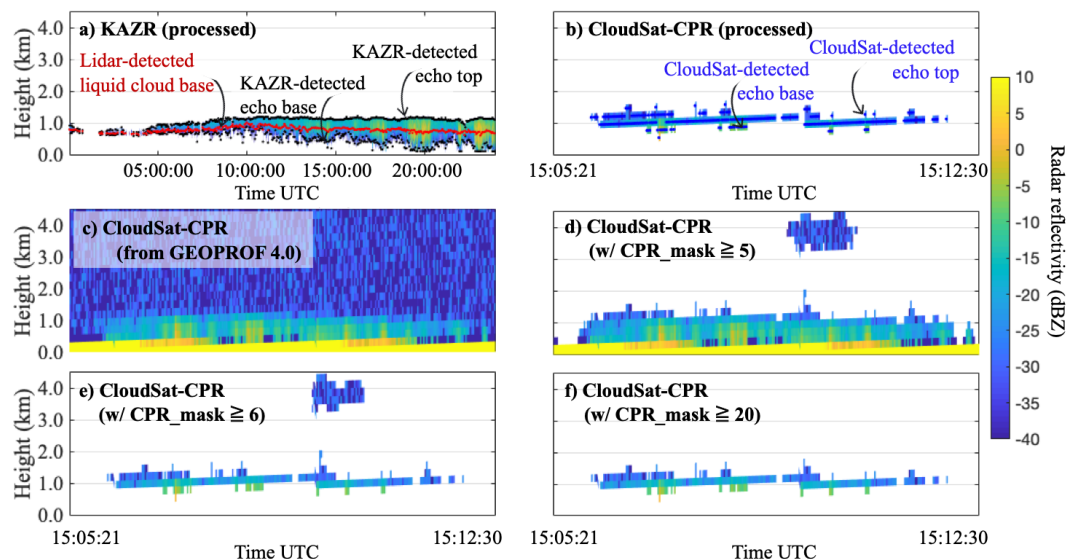
725 ** Across track dimension is not represented

726



727 **Figures**

728



729

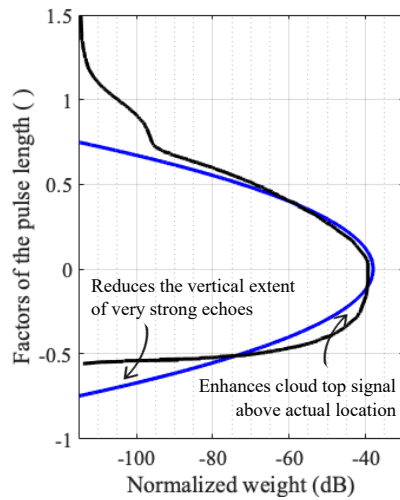
730 **Figure 1.** Hydrometeor radar reflectivity measured on Feb. 27, 2016 a) by KAZR and b) by the CloudSat-CPR when
731 it overpassed the KAZR located at the Eastern North Atlantic (ENA) observatory at 15:05:21 UTC. For KAZR, 24-
732 hrs of measurements are show. For CloudSat, a ground-track taken in ~7-sec is shown (a total length of ~3,000 km).
733 Dots on these figures represent the boundaries of the radar echo (black and blue dots for the KAZR and the CloudSat-
734 CPR respectively) and the location of the ceilometer-determined cloud base (red dots). Also plotted are the CloudSat
735 radar reflectivity c) raw, d) for significant returns ($CPR_mask > 5$), e) for echoes deemed very weak and stronger
736 ($CPR_mask > 6$) and f) for echoes deemed weak and stronger ($CPR_mask > 20$).

737

738

739

740



741

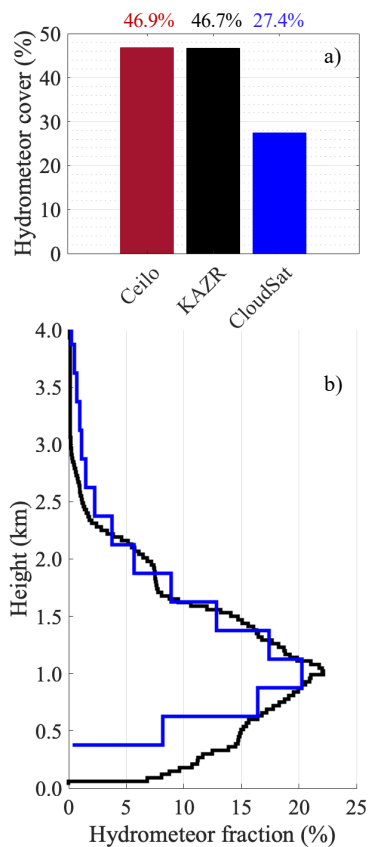
742 **Figure 2.** Symmetrical (blue) and asymmetrical (black) range weighting functions for the forward simulated radar
743 architectures detailed in Table 1.

744

745

746

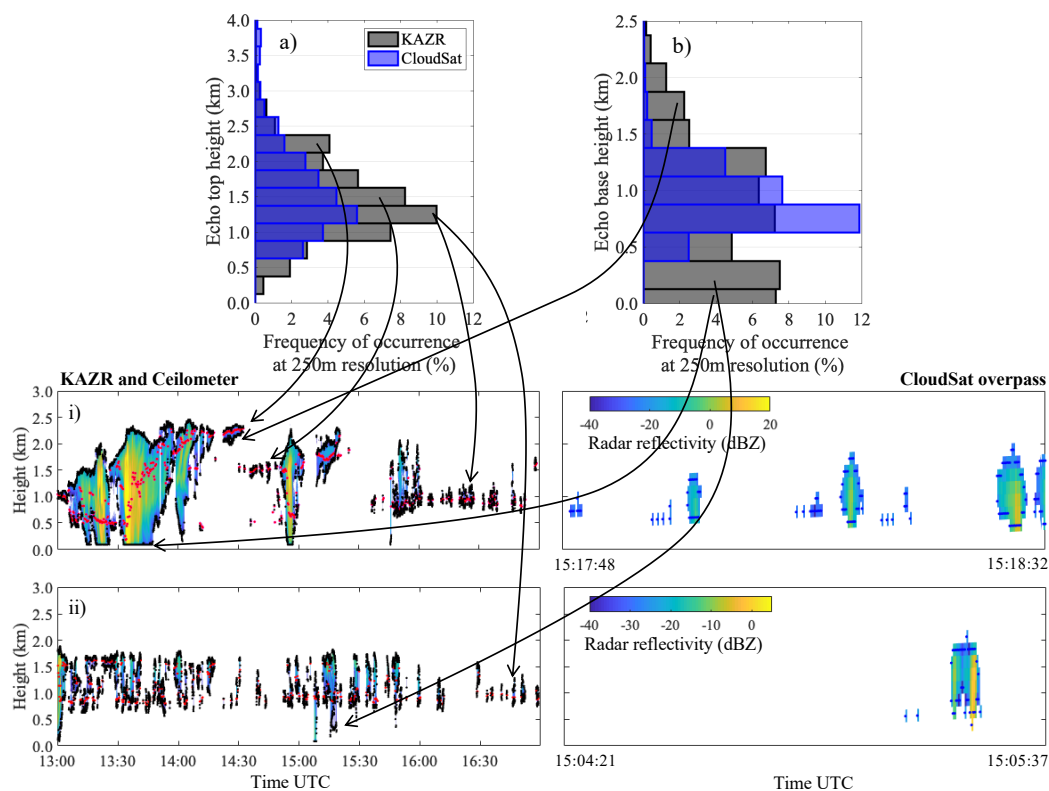
747



748

749 **Figure 3.** For 89 days where CloudSat overpassed the ENA observatory, a) fraction of observed profiles with cloud
750 or rain (i.e., hydrometeor cover) and b) hydrometeor fraction profile. Both estimated from CloudSat-CPR observations
751 (blue) and ground based KAZR observations during the 4-hr time window when CloudSat overpassed the KAZR
752 (black).

753



754

755 **Figure 4.** For 89 days where CloudSat overpassed in the vicinity of the ENA observatory, distribution of a) echo base
 756 height, and b) echo top height, estimated from CloudSat-CPR observations (blue) and ground-based KAZR
 757 observation during the 4-hr time window when the CloudSat-CPR overpassed the KAZR (grey). For references are
 758 examples of hydrometeor radar reflectivity measured on i) Feb. 02, 2017 and ii) Oct. 24, 2016 by the ground based
 759 KAZR and by the CloudSat-CPR. Dots on these figures represent the boundaries of the radar echo (black and blue
 760 dots for the KAZR and the CloudSat-CPR respectively) and the location of the ceilometer-determined cloud base (red
 761 dots).

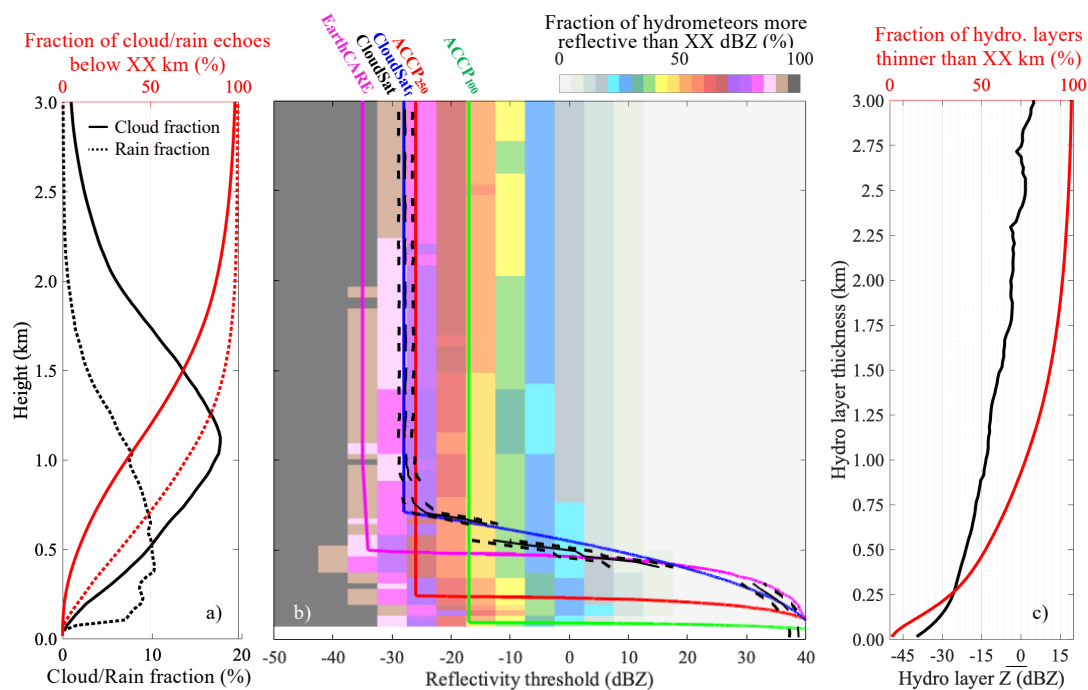
762

763

764

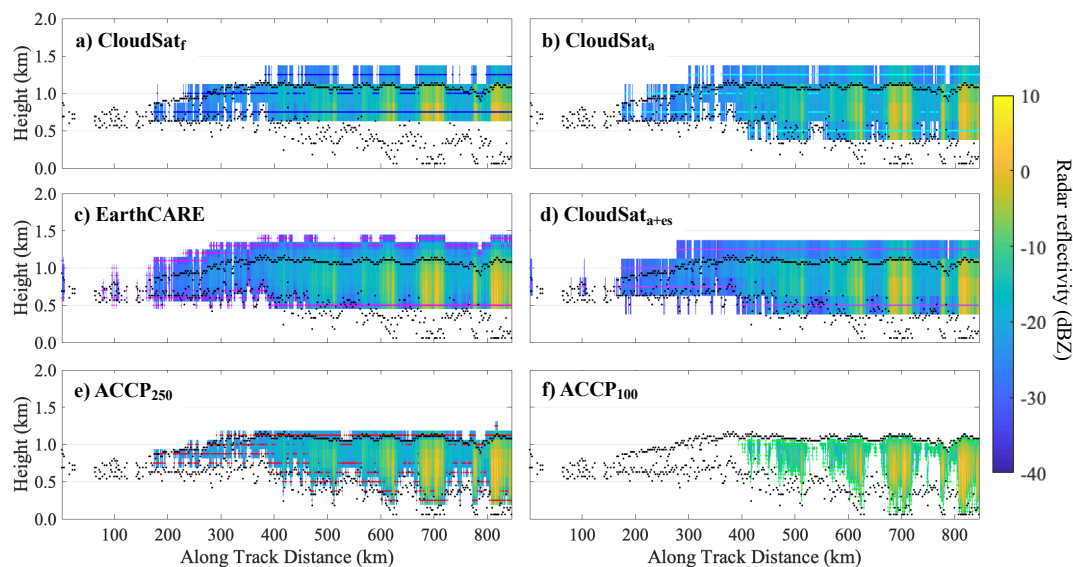
765

766



767
 768
 769
 770
 771
 772
 773
 774
 775
 776
 777
 778
 779

Figure 5. From ground based KAZR observations collected between 10/2015 and 02/2018, a) profile of cloud (solid black line) and sub-cloud layer rain (dotted black line) fraction, and the fraction of either cloud (solid red line) or sub-cloud-layer rain (dotted red line) echoes located below of certain height. b) Fraction of hydrometeor (cloud or rain) echoes with reflectivity larger than a given reflectivity threshold (colormap) with superimposed the surface clutter profile as simulated for the CloudSat (royal blue line) EarthCARE (magenta line), ACCP₂₅₀ (red line) and ACCP₁₀₀ (green line) CPR configurations and as observed by the CloudSat-CPR between May 2010 and November 2017 (broken black line marks the median, dotted black lines mark the interquartile range); c) median profile of hydrometeor layer mean reflectivity as a function of thickness (black) and the fraction hydrometeor (cloud and rain) layers thinner than a certain thickness (red).



780

781 **Figure 6.** Based on KAZR observations of the hydrometeor layer of Feb. 27, 2016, forward simulated radar reflectivity
782 (colormap) and estimated hydrometeor layer boundaries (colored dots) for a) CloudSat_r (royal blue dots), b)
783 CloudSat_{mps} which is CloudSat operating with the EarthCARE asymmetrical range weighting function (cyan dots), d)
784 CloudSat_{mps+es} which additionally has an enhanced sensitivity equivalent to the EarthCARE (purple dots), c)
785 EarthCARE which additionally operates with a factor of 5 vertical oversampling (magenta dots), e) ACCP₂₅₀ which
786 instead has a 250-m range resolution (red dots) and f) ACCP₁₀₀ which instead has a 100-m range resolution (green
787 dots). For reference, the corresponding KAZR observed radar reflectivity are depicted in Fig. 1a and echo boundaries
788 identified by the KAZR are overlaid on each subpanel using black dots.

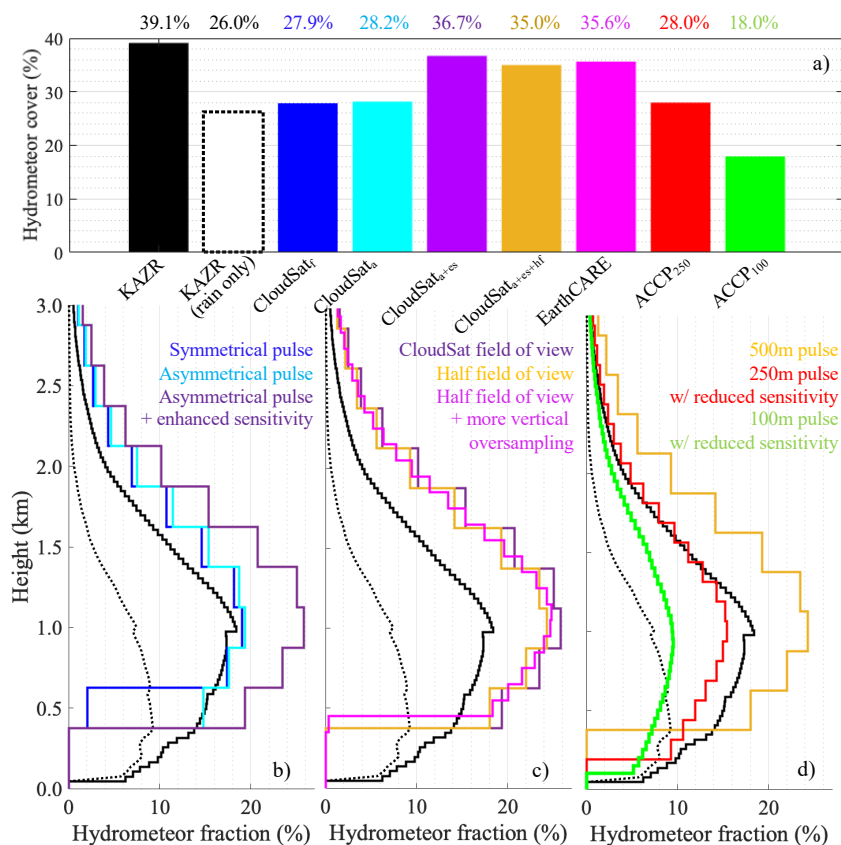
789

790

791

792

793



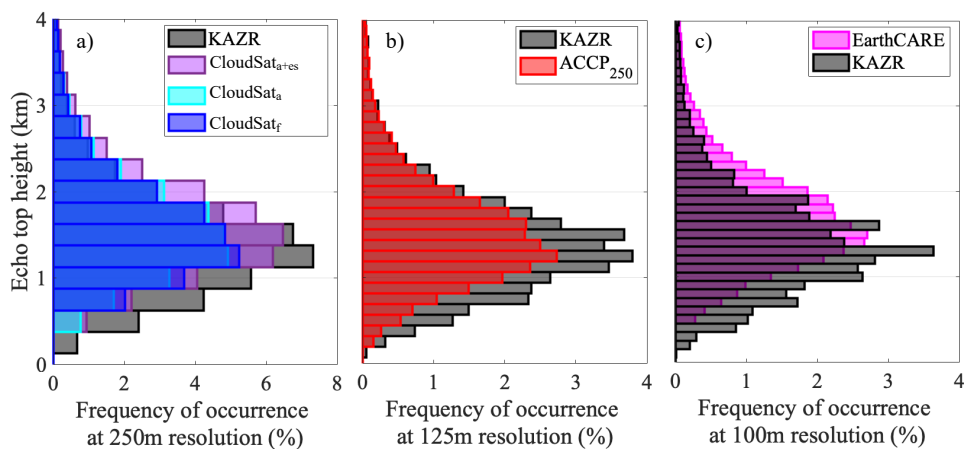
794

795 **Figure 7.** For 719 forward simulated days: a) fraction of observed profiles containing either cloud or rain (i.e.,
 796 hydrometeor cover); Also, for KAZR only, using complementary ceilometer observations, we estimate the fraction of
 797 all observed profiles containing rain in the sub-cloud layer. b-c-d) hydrometeor fraction profile estimated for all the
 798 forward-simulated radar architectures. All acronyms and colors are defined in Fig. 6 with the exception of
 799 CloudSat_{ts+es+hf} which is the CloudSat operating with EarthCARE’s asymmetrical range weighting function,
 800 enhanced sensitivity and half the horizontal field of view (gold).

801

802

803



804

805 **Figure 8.** For 719 forward simulated days, distribution of echo top height observed by KAZR (grey) and estimated
806 from the forward simulated radar architectures. Results are estimated at various range sampling resolutions according
807 to the capability each spaceborne sensor configuration. All acronyms and colors are defined in Fig. 6.

808

809

810